Production of maximilly aligned O(1D) atoms from two-step photodissociation of molecular oxygen.

Eppink, A.T.J.B.; Parker, D.H.; Janssen, M.H.M.; Buijsse, B.; van der Zande, W.J.

published in
Journal of Chemical Physics
1998

DOI (link to publisher)
10.1063/1.475502

document version
Publisher's PDF, also known as Version of record

Angular distributions for photodissociation of O_2 in the Herzberg continuum

B. Buijsse and W. J. van der Zande
FOM Institute for Atomic and Molecular Physics, Kruislaan 407, 1098 SJ Amsterdam, The Netherlands

A. T. J. B. Eppink and D. H. Parker
University of Nijmegen, Department of Molecular and Laser Physics, Toernooiveld 1, 6525 ED Nijmegen, The Netherlands

B. R. Lewis and S. T. Gibson
Research School of Physical Sciences and Engineering, The Australian National University, Canberra, ACT 0200, Australia

(Received 15 December 1997; accepted 27 January 1998)

Photodissociation in the Herzberg continuum of molecular oxygen has been studied at 236, 226 and 204 nm. Using ion-imaging and monitoring of $O(^3P_j)$, $j=0$, 1, and 2 product-atom angular distributions, the amount of parallel character of the transition was measured. In order to interpret these data, analyses of the photoabsorption oscillator strengths and the parallel-perpendicular nature of the Herzberg I, II and III bands, and extrapolation of these properties into the Herzberg-continuum region have been performed. Our measured fine-structure-averaged angular distributions are found to be consistent with this photoabsorption model. In addition, the dynamics of the dissociation process is discussed, based on the O-atom fine-structure distributions. © *1998 American Institute of Physics.* [S0021-9606(98)01317-8]

I. INTRODUCTION

Photodissociative reactions of diatomic molecules yield atoms that may either be in the ground state or in an excited state. Not only the quantum state of each atom, but also the photofragment angular distribution is an important observable. In particular, the angular distribution can elucidate the amount of parallel ($\Delta\Lambda=\Delta\Omega=0$) and perpendicular ($\Delta\Lambda=\Delta\Omega=\pm1$) character in an electronic transition to a continuum state, information that is unattainable using conventional spectroscopic techniques. In contrast to the case of dipole-allowed transitions, where one matrix element dominates the transition probability, the situation is different for the weaker forbidden transitions. Here, intensity is borrowed from allowed transitions through one or several second-order pathways with either parallel or perpendicular character. If the nature of the optical excitation is a mixture of parallel and perpendicular, then this will be reflected in the photofragment angular distribution. In this way, angular distributions form a diagnostic tool which is of particular interest in the study of forbidden bound-free transitions. In this paper, we use this tool for investigation of the photodissociation of molecular oxygen in the Herzberg continuum.

The structure of molecular oxygen is complicated. This, for example, is reflected in the fact that oxygen has six bound states below the first dissociation limit, all correlating with ground-state $O(^3P_j)$ product atoms: the ground state $X\ ^3\Sigma_g^-$ and five metastable states, labelled $a\ ^1\Delta_g$, $b\ ^1\Sigma_g^+$, $A\ ^3\Sigma_u^+$, $c\ ^1\Sigma_u^-$, and $A'\ ^3\Delta_u$. The Herzberg transitions are electric-dipole-forbidden transitions from the O_2 $X\ ^3\Sigma_g^-$ ground state to the $A\ ^3\Sigma_u^+$, $c\ ^1\Sigma_u^-$, and $A'\ ^3\Delta_u$ states.[1–3] In our earth's atmosphere, the large abundance of oxygen compensates for the forbidden character of these transitions, and their importance to aeronomy[4] and atmospheric photochemistry[5] has made the Herzberg transitions the subject of considerable study. However, progress in characterizing the spectroscopy of these states has been slow, due to the weakness of the Herzberg I ($A\ ^3\Sigma_u^+\leftarrow X\ ^3\Sigma_g^-$), Herzberg II ($c\ ^1\Sigma_u^-\leftarrow X\ ^3\Sigma_g^-$), and Herzberg III ($A'\ ^3\Delta_u\leftarrow X\ ^3\Sigma_g^-$) transitions, and also because of the strong pressure dependence of the Herzberg III transition intensity.[6,7] Understanding the spectroscopy requires detailed knowledge of the transition dipoles, to be discussed in detail in Sec. IV C. Briefly, the oscillator strength of the Herzberg transitions, including the corresponding dissociation continuum, is borrowed from dipole-allowed transitions through spin-orbit and orbit-rotation interactions, leading to an overall transition of mixed parallel and perpendicular character.

It is principally the Herzberg continuum that is responsible for photodissociation of O_2 in the 200–240 nm region. We have employed the technique of photofragment imaging to measure the angular distribution of the photofragments at 236, 226 and 204 nm. Hence, we have been able to determine the parallel-perpendicular nature of the transition to the Herzberg continuum at these wavelengths, assuming axial recoil for the (instantaneous) dissociation process. An expectation of the photofragment angular distributions can be obtained from an understanding of the discrete spectroscopy of the Herzberg systems. We have reviewed the current experimental and theoretical state of knowledge on the Herzberg transitions in O_2, employing the best available molecular parameters in the construction of a model of the corresponding O_2 photoabsorption, both for the bound and the continuous parts of the spectrum. Calculated cross sections based on this model are then used to independently assess our angular dis-

tributions, testing the quality of our knowledge of the Herzberg transitions.

In addition, we have investigated the *adiabaticity* of the dissociation process. The dynamics of diatomic molecular dissociation affects the relative population of the fine-structure states of the atomic photofragments. In particular, if a molecular Born-Oppenheimer state has fine structure, as is the case for the A and A' states, then the dissociation dynamics determines how the population of the molecular fine-structure states redistributes itself over the fine-structure states of the atoms.[8] Photodissociation in the Herzberg continuum produces only ground-state ^3P_j atoms, with j either 0, 1 or 2. Our experimental setup enables fine-structure-resolved measurements, not only of the rate at which $O(^3P_j)$ atoms are formed, but also of the corresponding angular distributions. Whether a molecule adiabatically follows a particular potential-energy curve to dissociation, or undergoes transitions to neighboring potentials correlating with different atomic fine-structure limits, is related to the velocity with which the dissociating molecule probes these potentials. In this way, the dissociation dynamics affects the branching ratio over the atomic multiplet. In addition, as our results will show, the angular distribution may also differ for each fine-structure component if the fine-structure levels of an excited molecular state do *not* contribute equally to a particular fine-structure state of the atomic fragments.[9]

The molecular photodissociation dynamics can be characterized by an adiabaticity parameter,[10,11] $\xi = \Delta R \Delta E_{SO}/\hbar v$ which compares the recoil time $\Delta R/v$, where ΔR is a characteristic recoil distance and v is the recoil velocity, with the characteristic time for spin-orbit coupling $\hbar/\Delta E_{SO}$, where ΔE_{SO} is the asymptotic spin-orbit coupling. Two limiting cases, the sudden-recoil limit ($\xi \rightarrow 0$), and the adiabatic limit ($\xi \rightarrow \infty$), correspond to high and low recoil velocity, respectively.

In the sudden-recoil limit, the atomic multiplet distribution is often close to a statistical one, i.e. proportional to $2j+1$, the degeneracy of each j state. However, for an exact calculation of the fine-structure distribution in this limit, a frame transformation in which molecular eigenstates are expanded in atomic eigenfunctions is required.[8]

The other extreme is fully adiabatic behavior. In this case, the projection Ω on the internuclear axis, of the total angular momentum of the initial Born-Oppenheimer state, is conserved during dissociation. At small internuclear separation R, the electrostatic forces between the nuclei are high and L and S are coupled to the internuclear axis [Hund's case (a)]. At greater R, the spin-orbit coupling becomes dominant over the electronic term in the Hamiltonian, and L and S couple to each other, but Ω remains a good quantum number [Hund's case (c)]. An adiabatic correlation diagram[11] can be used to find the specific atomic fine-structure state that connects with the fine-structure level of the molecule, this procedure amounting to ignoring any couplings between the noncrossing case (c) potential-energy curves.

Reality is often intermediate between the limiting cases. In this situation, the couplings between different electronic states must be known accurately. At short R, spin-orbit couplings may induce diabatic transitions between case (a) potentials, while at large R, where the spin-orbit term is diagonalized in the case (c) description, nonintersecting case (c) potentials may be coupled nonadiabatically by terms such as the radial kinetic-energy operator or the **L**-uncoupling operator.[10] Accurate knowledge of the potential-energy curves and the strengths of the couplings must be available for calculation of the fine-structure branching in this general case.[11]

Several authors have studied fine-structure branching in the dissociation of O_2. Matsumi and Kawasaki,[12] and Huang and Gordon,[11] using resonance-enhanced multi-photon ionization (REMPI), and laser-induced fluorescence (LIF) detection of the photofragments, respectively, performed fragmentation experiments at 157 nm in the Schumann-Runge (SR) continuum where they measured principally $O(^3P_j)$ fragments with $j=2$. Photodissociation of O_2 slightly above threshold in the SR continuum has been shown to be fully adiabatic.[13] Matsumi and Kawasaki[12] have also measured fine-structure branching ratios and Doppler profiles in the SR bands at 193 nm, obtaining results intermediate between the sudden-recoil and adiabatic limits. Leahy *et al.*,[14,15] using fast-beam photofragment translational spectroscopy, have measured *correlated* $O(^3P_{j_1}) + O(^3P_{j_2})$ predissociation branching ratios for the SR bands, also obtaining results inconsistent with both the diabatic and adiabatic limits. Finally, Tonokura *et al.*[16] reached similar conclusions following the measurement of fine-structure branching ratios at 226 nm in the Herzberg continuum. Their results will be discussed in more detail in Sec. V A.

II. EXPERIMENT

Ion-imaging techniques have proven to be very valuable in the study of photodissociative processes. The full three-dimensional (3D) velocity distribution of recoiling fragments can be projected in one single image, revealing the kinetic-energy release in the dissociation process and the angular distribution of the photofragments. A detailed description of conventional ion imaging has been given in Ref. 17. A brief description of this technique and the experimental velocity-mapping setup that we used[18] will be presented here.

As depicted schematically in Fig. 1, the vacuum system consists of differentially-pumped source and ionization chambers. A cold, pulsed molecular beam is obtained by a supersonic expansion of 10%–20% O_2 in He as carrier gas at a stagnation pressure of 2 bar. We estimate the temperature of the beam to be between 5 and 10 K, implying an O_2 ground-state population predominantly in the lowest rotational level. Subsequently, the beam enters the ionization chamber through a 1 mm skimmer, passes a 1 mm hole in a repeller electrode, and is crossed at right angles by two pulsed, counter-propagating focused laser beams, one beam for pumping the Herzberg continuum, the other for probing the nascent oxygen atoms by means of REMPI. The atomic ions are formed in the presence of an electric field between the repeller and extractor plates ($V_E/V_R \approx 0.7$; $V_R \approx 4000$ V), and accelerated along the axis of a time-of-flight (TOF) tube towards the detector. These ions travel on expanding, nested

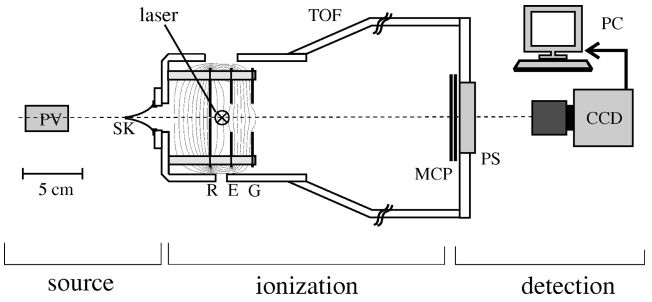

FIG. 1. Velocity-map imaging experimental setup: PV=pulsed valve; SK=1 mm skimmer; axially symmetric ion optics with Rm=repeller at voltage V_R, E=extractor at voltage V_E and G=ground electrode; a 15 mm spacing between the 0.2 mm thick plate electrodes is set using aluminum oxide tubes; E and G contain 20 mm apertures such that equipotential surfaces are bent as indicated; ⊗ denotes the laser focus, 108 mm downstream from the nozzle; TOF tube, 36 cm from laser focus to detector; dual MCP detector with PS=phosphor screen; CCD camera connected to the PC.

spherical surfaces, where the expansion speed of each surface is determined by the kinetic-energy release in the corresponding dissociation channel.

The extractor plate is part of the ion-lens optics, consisting of an axially symmetric three-plate assembly, with 20 mm apertures in the extractor and ground electrodes, thus forming an asymmetric immersion lens.[18] This lens guides all particles with the same initial velocity vector to the same point on the detector, irrespective of their initial distance from the ion-lens axis, a technique called *velocity-map imaging*.[18,19] The result is a better spatial resolution than in conventional ion imaging where an extracting wire-grid electrode is used. A good resolution is crucial in the two-laser experiments described here, in order to discriminate between the different images on the detector.

In the TOF tube, a separation takes place between ions of different masses. Simultaneously, the spherical distribution of fragment ions is flattened by the acceleration along the TOF axis in such a way that the spread in time-of-flight $\Delta t/t$ is very small ($<1\%$). This enables mass-selective ion detection with an imaging detector [dual 40 mm microchannel-plates (MCP) with a P-20 phosphor screen] by the application of a timed voltage pulse to the front MCP. The two-dimensional images appearing on the phosphor screen are recorded by a CCD camera equipped with a 25 mm focal-length objective lens. Images are integrated on the CCD chip over a preset number of laser pulses, and subsequent images are summed in a PC where further data analysis is performed. By choosing the polarization vector of the dissociation laser parallel to the image plane, the so-called inverse Abel-transform method[20] can be used to reconstruct the original 3D velocity distribution.

The Herzberg states, A, A', and c, all correlate with the $O(^3P_{j_1})+O(^3P_{j_2})$ dissociation limit. Adiabatically, these states connect to one fine-structure dissociation limit with $j_1=j_2=2$. State-selective detection of the individual $O(2p\ ^3P_j)$ atoms is achieved by $(2+1)$ REMPI through the $O(3p\ ^3P_{j'})$ states, using wavelengths of 226.233, 226.059 and 225.656 nm for $j=0$, 1, and 2, respectively. For this purpose, a Nd:YAG-pumped dye laser (Spectra-Physics DCR-2A and PDL-2), operated with Coumarin-460 dye and frequency doubled in a BBO crystal, is used. In principle, about 0.5 mJ/5 ns UV power with vertical polarization (i.e., parallel to the detector face) can be focused onto the molecular beam with a lens of 20 cm focal-length. In order to avoid space-charge problems, the UV power is attenuated to about 0.1 mJ/5 ns. In spite of the considerable laser fluence, the one-photon transition is far from saturated. At the peak of the Herzberg continuum, where the absorption cross section is 7.35×10^{-24} cm^2, we dissociate about 1 in 10^5 molecules. Furthermore, the detection laser is scanned back and forth over the REMPI transition during image-data acquisition, thus probing all velocity groups at equal sensitivity and avoiding Doppler selection. Due to this scanning process, the fine-structure of the intermediate $O(3p\ ^3P)$ state is not resolved. The integrated two-photon line strengths are reported to yield equal sensitivity for the initial fine-structure states,[21–24] which simplifies the study of branching between these states. Since the $O(^3P_j)$ REMPI wavelengths are also suitable for excitation of O_2 into the Herzberg continuum, we performed, in the first instance, single-laser experiments. Images obtained with the molecular beam triggered after the laser pulse have been used to subtract the contribution of thermalized ambient background gas.

In the two-laser experiments, a second Nd:YAG-pumped dye laser (Spectra-Physics GCR-11 and PDL-2) is used to generate excitation wavelengths in the 203–240 nm range. The ~204 nm light is produced by frequency doubling and mixing in KDP and BBO crystals the output of the dye laser operated with Sulforhodamine 640 dye. Longer wavelengths are produced by direct frequency doubling in a BBO crystal, using the third harmonic of the YAG laser to pump, e.g., Coumarin-480 dye. In order to obtain vertical polarization, a Berek's compensator is used. Images from each laser separately are subtracted from the images with both lasers present, yielding the double-resonant signal free from background. The UV power was balanced and the focal points of the two laser beams were overlapped carefully in order to maximize the double-resonant signal while maintaining a homogeneous detection efficiency.

III. RESULTS

In Fig. 2(a), a raw O^+ ion image from $O(^3P_2)$ REMPI at 225.66 nm is shown. Three rings appear: the inner ring corresponding to one-photon excitation into the Herzberg continuum, leading to $O(^3P_2)+O(^3P_j)$; the middle ring and the outer ring due to two-photon excitation, leading to $O(^3P_2)+O(^1D_2)$ (second dissociation limit) and $O(^3P_2)+O(^3P_j)$, respectively. The reconstructed image, Fig. 2(b), represents a vertical section through the 3D distribution, and is obtained by an inverse Abel transform of the raw image. From this image, the 3D speed distribution in Fig. 3(a) is obtained by integrating over all angles, the results of which represent the branching between the three dissociation channels. The middle ring is strongest at this wavelength. In contrast, for the $j=0$ and $j=1$ images, the two-photon transition is much weaker. The reason for this rapid intensity variation with wavelength is the presence of quasi-bound Rydberg states at the two-photon energy.[19] At 225.66 nm, the $3d\delta\ ^3\Pi_{0,1}(v=2)$ state[25] enhances the two-photon excitation strength. This

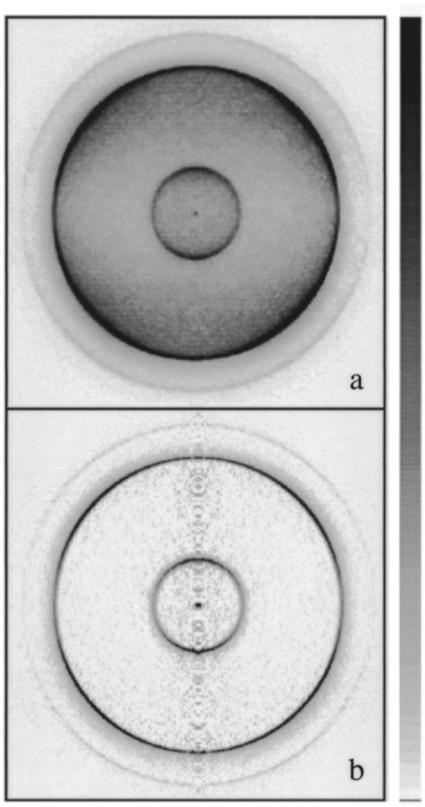

FIG. 2. (a) Raw $O(^3P_2)$ ion image obtained using a single laser at a wavelength near 225.67 nm. During 10 000 laser shots of data acquisition, the wavelength was scanned back and forth (by ~0.03 nm) across the REMPI transition. Laser polarization was vertical in the image, and the laser propagation direction was from left to right. The center dot corresponds to the O_2^+ signal at zero kinetic energy which is strong enough to be seen outside of the mass-selective gate for O^+. (b) Corresponding reconstructed image obtained by means of an inverse Abel transform. The 3D velocity distribution is recovered by revolution of the image around the vertical symmetry axis.

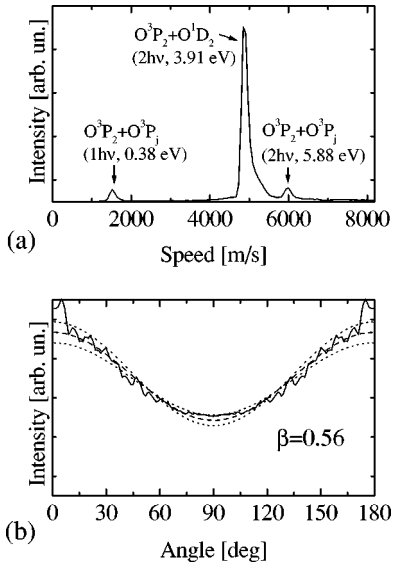

FIG. 3. Speed and angular distributions obtained from Fig. 2(b). (a) The speed distribution shows three channels, the outer two fast channels corresponding to two-photon excitations, and the slow channel to one-photon excitation into the Herzberg continuum. Dissociation limits and kinetic energy releases for each channel are indicated. (b) The angular distribution of the inner ring for this experimental run (solid curve) is fitted with $\beta=0.56$ (dashed curve), indicative of the dominance of parallel character in the excitation process. For comparison, curves with $\beta=0.46$ and 0.66 are shown also.

state subsequently predissociates to the $O(^3P_2)+O(^1D_2)$ dissociation limit. This channel shows a distinct quadrupolar angular distribution, indicative of $\Sigma\rightarrow\Sigma\rightarrow\Pi$ or $\Sigma\rightarrow\Pi\rightarrow\Pi$ two-photon transitions, for which the angular distribution is described by $I(\theta)\propto 1+\beta P_2(\cos\theta)+\gamma P_4(\cos\theta)$, where P_2 and P_4 represent second- and fourth-order Legendre polynomials, respectively, β and γ are anisotropy parameters, and θ is the angle between the recoil and laser-polarization directions. The outer ring is much weaker: apparently predissociation to the lower dissociation limit is weak.[26]

The inner ring corresponds to one-photon excitation into the Herzberg continuum, leading to $O(^3P_2)+O(^3P_j)$ at 0.38 eV kinetic-energy release. The angular distribution of these fragments is described by the simpler $I(\theta)\propto 1+\beta P_2(\cos\theta)$ distribution. This ring is quite weak due to the electric-dipole-forbidden nature of the Herzberg transitions. The character of the Herzberg transition will be discussed in detail in Sec. IV. Here, the statement that the transition borrows oscillator strength by mixing with other electronic states both in the ground and in the excited state will suffice. The transition strength comprises two types of contribution, parallel and perpendicular, for which $\beta=2$ and -1, respectively. Since the dissociation process takes place on a time scale much shorter than molecular rotation, the fragment angular anisotropy reflects directly the relative importance of the parallel and perpendicular contributions to the transition. In Fig. 3(b), the angular distribution measured for the inner ring is displayed, together with a fitted curve (dashed line) yielding an anisotropy parameter $\beta=0.56$ for this experimental run, and indicative curves (dotted lines) for $\beta=0.46$ and 0.66.

In this study, we concentrate solely on the Herzberg continuum, i.e. the one-photon signal. In Table I, the experimentally determined β parameters for the inner ring are listed. The tabulated values, classified according to three main excitation wavelengths (204, 226 and 236 nm), represent average fitted β parameters determined over a series of images. The uncertainty listed is, therefore, the standard deviation from the mean value, which is found to dominate the uncertainty resulting from the fitting procedure for a single image. The two main sources of error are believed to be associated with the method for background subtraction, and long- and short-term variations in detector sensitivity.

TABLE I. Measured anisotropy parameters β, characterizing the angular distribution of photofragments formed in the excitation of the O_2 Herzberg continuum at 204, 226, and 236 nm. Atoms are formed in three fine-structure states $O(^3P_j)$, with $j=0$,1 and 2.

λ	β		
nm	$j=0$	$j=1$	$j=2$
204	0.35±0.15	0.53±0.15	0.87±0.10
226	0.37±0.24	0.61±0.09	0.64±0.08
236	-	0.31±0.15	-

For the one-laser experiment, the dissociation branching ratio over the different fine-structure states could only be determined at 226 nm. The measured $j=0:1:2$ branching ratio, normalized to the $j=0$ intensity, is $1.00\pm0.26:3.33\pm0.43:9.00\pm0.70$. These results have been corrected for the effects of the slight variation in laser intensity at the three detection wavelengths for $j=0$, 1, and 2. Reliable branching ratios could not be obtained for the two-laser experiments (dissociation at 204 nm and 236 nm, detection at 226 nm) because the signal in these cases relies on the precise overlap of the focal points of the two lasers: the three detection wavelengths lie relatively far apart, and when scanning the detection-laser wavelength, dispersive elements in the optics chain cause a significant displacement in the detection-laser focal position. Relative measurements, such as the angular distribution for different j states at 204 nm and 236 nm, are not affected by this overlap problem. For 236 nm measurements, however, the strong signal created by the 226 nm detection laser, especially for $j=2$, overwhelms the weak dissociation-laser signal. Only the $j=1$ signal from 236 nm dissociation could be extracted reliably from the detection-laser background.

IV. THE HERZBERG TRANSITIONS

A. Previous work

As explained in Sec. I, the angular distribution of the photofragments is closely related to the nature of the Herzberg continuum. Understanding the Herzberg continuum requires a thorough knowledge of the Herzberg bands. The discrete spectroscopy of the Herzberg states has been reviewed comprehensively by Slanger and Cosby,[27] with the review based principally on the high-resolution, multiple-reflection cell spectrographic measurements performed at the Herzberg Institute of Astrophysics, Ottawa.[28–31] Since the time of the Slanger and Cosby review, significant new high-resolution measurements have been performed by Yoshino *et al.*[32] and Slanger *et al.*,[33] using ultraviolet Fourier-transform spectroscopy (UVFTS) and cavity ring-down spectroscopy (CRDS), respectively. At present, the spectroscopic constants of the A state are known, from absorption spectra, for $v=0-12$, those of the c state for $v=1-18$, and those of the A' state for $v=2-13$.[34] Knowledge of the absolute and relative intensities of the Herzberg transitions is far from complete however, most of the early estimates being based on spectrographic data. Recently, Huestis *et al.*[35] published experimental oscillator strengths for the (8,0)–(11,0) bands of the $A\leftarrow X$ system, the (13,0), (14,0) and (16,0) bands of the $c\leftarrow X$ system, and the (9,0) and (11,0) bands of the $A'\leftarrow X$ system, based on CRDS in absorption, while Yoshino *et al.*[36] have measured oscillator strengths for the (4,0)–(11,0) bands of the $A\leftarrow X$ system using UVFTS. At present, it appears that the most reliable Herzberg I oscillator strengths are those of Yoshino *et al.*[36] However, the $c\leftarrow X$ and $A'\leftarrow X$ oscillator strengths of Huestis *et al.*[35] must be regarded as the only reasonable data available on the strengths of the Herzberg II and III transitions, despite the acknowledged shortcomings of CRDS in providing quantitative intensity information.[33,35] From their measured discrete oscillator strengths, Huestis *et al.*[35] concluded that the Herzberg I transition provides $\sim$86% of the total strength of the Herzberg transitions.[37] To obtain an improved estimate of this quantity, it would be useful to have measurements of the Herzberg II and III oscillator strengths of the same resolution and quality as the Herzberg I UVFTS measurements of Yoshino *et al.*[36]

Measurement of the small Herzberg continuum cross section is a difficult problem, complicated not only by the necessity to extrapolate to zero pressure in order to remove the effects of collisional enhancement of the Herzberg III cross-section component, but also by corrections for the effects of Rayleigh scattering and the predissociation line wings of the nearby SR bands, $B\,^3\Sigma_u^-\leftarrow X\,^3\Sigma_g^-$. Direct, long-path measurements of stratospheric transmittances demonstrated that most of the early measurements had overestimated the cross section by as much as 40%.[38–40] This inspired new laboratory measurements[41–43] that confirmed a lower cross section. However, there remained differences between the results obtained in different laboratories from measurements taken with different path lengths and pressures, and it was not until the work of Yoshino *et al.*[44] that these differences were reconciled, resulting in a single recommendation for the Herzberg continuum cross section and its pressure dependence. In this work, we will adopt this recommendation for the absolute value of the Herzberg continuum cross section, but we note that more recent measurements[45,46] have resulted in even lower values. Thus, the question of the magnitude of the Herzberg continuum cross section cannot be regarded as settled completely.

There have been several *ab initio* studies of the potential-energy curves of the A, c, and A' states, with the recent multireference configuration-interaction with Davidson correction (MRCI+Q) calculations of Partridge *et al.*[47] expected to be the most accurate. These calculations show differences in equilibrium internuclear distance R_e from experiment of only $\sim$0.005 Å, compared, for example, with first-order configuration-interaction calculations[48] which differ by $\sim$0.04 Å. As far as we are aware, there has been only one *ab initio* study, by Klotz and Peyerimhoff,[49] on the origin of the electronic transition moments for the Herzberg transitions, a challenging theoretical problem. Their study, restricted to a consideration of transition-strength gain from dipole-allowed transitions through spin-orbit interactions, predicted that the $A\leftarrow X$ transition is of mixed parallel-perpendicular nature (principally parallel), while the $c\leftarrow X$ and $A'\leftarrow X$ transitions are entirely perpendicular. Further studies of rotational line strengths in the Herzberg I (Refs. 35, 50) and III (Refs. 31, 35) bands have shown that orbit-rotation couplings produce detectable J-dependent contributions to the corresponding effective electronic transition moments. Herzberg continuum cross sections[51] and transition probabilities[52] calculated using the electronic transition moments of Klotz and Peyerimhoff,[49] are in only fair agreement with the best experimental results.[50]

In summary, it is clear that, despite a considerable body of work on the Herzberg transitions, many uncertainties remain. In particular, it has not been possible, using traditional spectroscopic techniques, to make direct measurements of

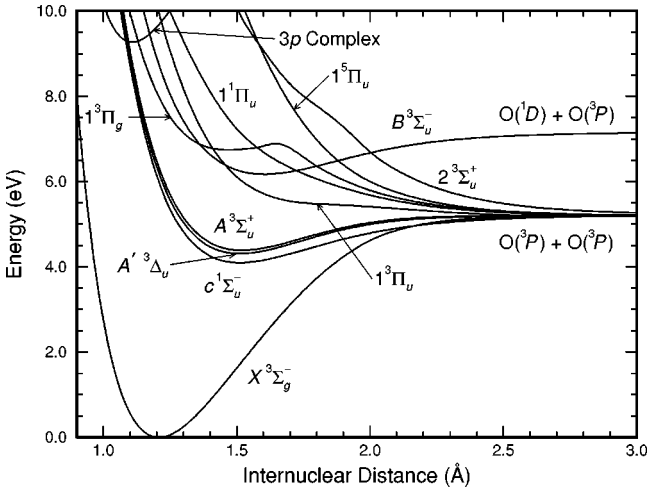

FIG. 4. Potential-energy curves of O_2 relevant to a discussion of the Herzberg transitions.

the branching ratios into the Herzberg I, II and III transitions which constitute the Herzberg continuum.

B. Potential-energy curves

Our adopted potential-energy curves for the A, A', and c states are shown in Fig. 4.[53] In principle, calculations of cross sections for the Herzberg continua, which peak near 6 eV, require significant extrapolations of the inner limbs of the potential-energy curves, away from the more accurately known bound-state potentials which have a common dissociation limit at $\sim$5.2 eV. However, it is possible both to extrapolate reliably using information from *ab initio* calculations, and, in some cases, to reduce the reliance on extrapolation by incorporating knowledge gained from experimental information on the Rydberg-valence interactions involving the Herzberg states.

Our adopted potential-energy curve for the A state was obtained using the following three-stage procedure. First, a Rydberg-Klein-Rees (RKR) (Ref. 54) potential-energy curve was constructed using the spectroscopic constants of Borrell *et al.*,[28] for $v=0-3$, and Yoshino *et al.*,[32] for $v=4-11$.[55] Second, the RKR potential curve was extended smoothly beyond the experimentally known region. The outer-limb extension was of the form[56]

$$V(R)=V_\infty-C_n/R^n, \tag{1}$$

where the exponent n and the coefficient C_n were determined using the last two RKR turning points and the known dissociation limit $V_\infty=5.2141$ eV$(=D_e)$.[57] Due to irregularities in the upper part of the inner limb of the RKR potential, it was necessary to begin the inner-limb extension at $\sim$5.05 eV ($v\approx9$). An initial extension was achieved by using the MRCI+Q potential of Partridge *et al.*,[47] shifted and scaled to agree as closely as possible with the RKR potential below $v=9$. The quality of this MRCI+Q potential can be judged by noting that it was necessary only to increase the well depth by 2.7%, shift to smaller R by 3.2 mÅ, and expand about R_e by 1.2% in order to obtain agreement with the RKR potential. Third, the inner limb of the A-state potential-energy curve in the 9–10 eV region was defined by using the results of a recent study of predissociation in the $3p\pi_u$ $D\,^3\Sigma_u^+$ Rydberg state,[58] represented qualitatively by the $3p$-complex potential-energy curve in Fig. 4. Briefly, the D state is predissociated *indirectly* by the $B\,^3\Sigma_u^-$ state, the upper state of the SR system, and *directly* by the A state. Banerjee[58] has performed a coupled-channel Schrödinger-equation analysis of the observed predissociation pattern which allows the repulsive limb of the A state, in the crossing region with the D state, to be defined quite accurately and the Rydberg-valence coupling between the A and D states of $^3\Sigma_u^+$ symmetry to be estimated. His results imply that the A-state potential-energy curve crosses that of the D state at $R=1.091$ Å, with a slope of -36 eV/Å, and that the Rydberg-valence coupling is 0.052 eV ($\simeq400$ cm^{-1}), much weaker than in the well-known case of the isoconfigurational $^3\Sigma_u^-$ states.[59] Finally, the MRCI+Q A-state inner limb, adjusted as described above, was extrapolated smoothly above $\sim$7 eV in order to be consistent with these new results. It was found that a short spline extrapolation above 8.9 eV of the modified *ab initio* inner limb was almost identical in the 9–10 eV region with the potential determined independently from the D-state predissociation studies,[58] leading to confidence in our inner-limb extension procedures.

Our adopted potential-energy curves for the A' and c states were determined by a similar procedure. However, for these states there is insufficient experimental information available on the predissociation of Rydberg states of like symmetry to enable their inner limbs to be defined more accurately in the 9–10 eV region than is possible using the *ab initio* modification techniques described above.[60] In the case of the A' state, an RKR potential-energy curve was constructed using the spectroscopic constants of Coquart and Ramsay[30] for $v=2-11$.[55] The inner-limb extension above $\sim$5.05 eV ($v\approx10$) was obtained by modifying the MRCI+Q A'-state potential of Partridge *et al.*[47] to optimize agreement with the RKR potential. This required an increase in well depth of 2.5%, a shift to smaller R by 4.1 mÅ, and an expansion about R_e by 0.8%. In the case of the c state, an RKR potential-energy curve was constructed using the spectroscopic constants of Ramsay[29] for $v=1-16$.[55] The inner-limb extension above $\sim$5.05 eV ($v\approx15$) was obtained by modifying the MRCI+Q c-state potential of Partridge *et al.*[47] to optimize agreement with the RKR potential. This required an increase in well depth of 1.0%, a shift to smaller R by 7.8 mÅ, and a contraction about R_e by 1.2%.

C. Transition moments

The electric-dipole-forbidden Herzberg transitions borrow intensity from electric-dipole-allowed transitions of the oxygen molecule through, in principle, spin-orbit and orbit-rotation interactions with both the upper and lower states of each transition. In the general case, the effective electronic transition moment is of mixed parallel-perpendicular character, with a number of independent moments necessary to reproduce the observed rotational line strengths for the discrete transitions.

1. The $A\ ^3\Sigma_u^+ \leftarrow X\ ^3\Sigma_g^-$ transition

In a general treatment of $^3\Sigma^{\pm} \leftarrow {}^3\Sigma^{\mp}$ transitions,[61] thirteen independent moments have been found to govern the rotational line strengths. In the particular case of the Herzberg I transition, $A\ ^3\Sigma_u^+ \leftarrow X\ ^3\Sigma_g^-$, however, England *et al.*[50] found that only three independent moments were necessary to explain the measured line strengths.[36] In their first-order picture, the dominant sources of $A \leftarrow X$ transition strength are the allowed transitions $B\ ^3\Sigma_u^- \leftarrow X\ ^3\Sigma_g^-$ (parallel) and $A\ ^3\Sigma_u^+ \leftarrow 1\ ^3\Pi_g$ (perpendicular), through the interactions $B\ ^3\Sigma_u^- - A\ ^3\Sigma_u^+$ [spin-orbit (SO)] and $1\ ^3\Pi_g - X\ ^3\Sigma_g^-$ [spin-orbit and orbit-rotation (OR)], respectively. This conclusion is essentially in agreement with the *ab initio* study of Klotz and Peyerimhoff,[49] which, however, considered only spin-orbit interactions, and also with the study of Huestis *et al.*[35] The independent moments Z, Y and M arise through the following interactions:[62]

$$X\ ^3\Sigma_{g,\pm1}^- \overset{\parallel}{\rightarrow} B\ ^3\Sigma_{u,\pm1}^- \overset{\mathrm{SO}}{\leftrightarrow} A\ ^3\Sigma_{u,\pm1}^+ : Z_1 = Z, \tag{2}$$

$$X\ ^3\Sigma_{g,0^+}^- \overset{\mathrm{SO}}{\leftrightarrow} 1\ ^3\Pi_{g,0^+} \overset{\perp}{\rightarrow} A\ ^3\Sigma_{u,\pm1}^+ : Y_1 = Y, \tag{3}$$

$$X\ ^3\Sigma_{g,\pm1}^- \overset{\mathrm{SO}}{\leftrightarrow} 1\ ^3\Pi_{g,\pm1} \overset{\perp}{\rightarrow} A\ ^3\Sigma_{u,0^-}^+ : Y_0 = Y, \tag{4}$$

$$X\ ^3\Sigma_{g,0^+}^- \overset{\mathrm{OR}}{\leftrightarrow} 1\ ^3\Pi_{g,\pm1} \overset{\perp}{\rightarrow} A\ ^3\Sigma_{u,0^-}^+ : M_0 = M, \tag{5}$$

$$X\ ^3\Sigma_{g,\pm1}^- \overset{\mathrm{OR}}{\leftrightarrow} 1\ ^3\Pi_{g,\pm2} \overset{\perp}{\rightarrow} A\ ^3\Sigma_{u,\pm1}^+ : M_1 = M, \tag{6}$$

$$X\ ^3\Sigma_{g,\pm1}^- \overset{\mathrm{OR}}{\leftrightarrow} 1\ ^3\Pi_{g,0} \overset{\perp}{\rightarrow} A\ ^3\Sigma_{u,\pm1}^+ : M_1 = M. \tag{7}$$

The sum rule for the $A \leftarrow X$ rotational line strengths, arising from all fine-structure levels of the lower state with a given J, implies that the square of the effective electronic transition moment is given by[63]

$$M_{\mathrm{eff}}^2 = [Z^2 + 4Y^2 - 4M^2 + 6M^2 J(J+1)]/g'', \tag{8}$$

where $g''=3$ is the lower-state degeneracy, and the perpendicular:parallel ratio by

$$M_{\perp}^2 / M_{\parallel}^2 = [4Y^2 - 4M^2 + 6M^2 J(J+1)]/Z^2. \tag{9}$$

The transition moments in Eqs. (2)–(9) depend parametrically on R, and some depend on J through the orbit-rotation coupling. For simplicity, these dependences have been suppressed in the transition-moment notation.

The effective electronic transition moment may be related to a (J-dependent) band oscillator strength by the relation

$$f_{v'v''} = 3.038 \times 10^{-6} \nu |\langle \chi_{v'}(R) | M_{\mathrm{eff}}(R) | \chi_{v''}(R) \rangle|^2, \tag{10}$$

where $\chi_{v''}(R)$ and $\chi_{v'}(R)$ are the normalized discrete radial wavefunctions of the initial and final states, respectively, ν is the transition energy, in cm^{-1}, and $M_{\mathrm{eff}}(R)$ is in a.u. In the R-centroid approximation,[64] Eq. (10) becomes

$$f_{v'v''} = 3.038 \times 10^{-6} \nu q_{v'v''} M_{\mathrm{eff}}^2(R_{v'v''}), \tag{11}$$

where

$$q_{v'v''} = |\langle \chi_{v'}(R) | \chi_{v''}(R) \rangle|^2 \tag{12}$$

is the Franck-Condon factor, and

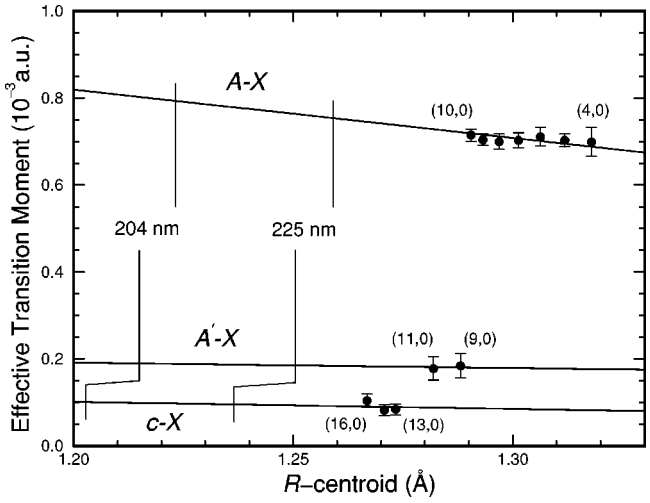

FIG. 5. Effective room-temperature electronic transition moments for the Herzberg transitions of O_2. Solid circles: values determined from measurements of the discrete oscillator strengths; $A \leftarrow X$ (4,0)–(10,0) (Ref. 50); $A' \leftarrow X$ (9,0), (11,0) and $c \leftarrow X$ (13,0), (14,0) and (16,0) (Ref. 35). Solid lines: adopted effective transition moments.

$$R_{v'v''} = \langle \chi_{v'}(R) | R | \chi_{v''}(R) \rangle / \langle \chi_{v'}(R) | \chi_{v''}(R) \rangle \tag{13}$$

is the R-centroid. Equation (11) can be used to determine an effective electronic transition moment, including an effective R dependence through association of R with the R-centroid, using experimental band oscillator strengths. As has been noted recently by Huestis,[65] there are complexities associated with degeneracy factors involved in the definition of transition moments for forbidden transitions. The effective electronic transition moments M_{eff}, defined by Eq. (11) and used self-consistently throughout this work, implicitly contain degeneracy factors which may make their definition inconsistent with some other studies.

We have used the values of Z ($\sim 1.0 \times 10^{-3}$ a.u.), Y ($\sim 0.4 \times 10^{-3}$ a.u.) and M ($\sim 0.01 \times 10^{-3}$ a.u.) determined by England *et al.*[50] from the measured absorption line oscillator strengths of Yoshino *et al.*[36] for the (4,0)–(10,0) $A \leftarrow X$ bands, with small adjustments to allow for the slightly different Franck-Condon factors arising from our A-state potential-energy curve, in Eq. (8) to determine values for the $A \leftarrow X$ effective electronic transition moment M_{eff}. The dependence of M_{eff} on the rotational quantum number leads to a temperature dependence of the corresponding absorption oscillator strength. We have evaluated M_{eff} for $J=11$, appropriate for calculation of room-temperature cross sections, and for $J=0$, appropriate for interpretation of the measurements of this work taken at rotational temperatures in the range 5–10 K. Our results for $J=1$ are shown in Fig. 5 (solid circles), plotted as a function of the $A \leftarrow X$ R-centroid.[66] When going from room temperature to the 5–10 K region, M_{eff}^2, and thus the absorption cross section, decreases by approximately 5% due to the J-dependent orbit-rotation coupling.

Calculations of the $A \leftarrow X$ photoabsorption continuum require a significant extrapolation of the effective transition moment towards smaller internuclear distances. Unfortunately, the precision with which such an extrapolation can be

performed, in the absence of other information, is limited. Therefore, as described further in Sec. IV D, we have chosen to use experimental information on the Herzberg continuum to further refine the transition-moment extrapolation. Our adopted effective $A \leftarrow X$ electronic transition moments are given by

$$M_{\mathrm{eff}}(R) = (2.154 - 1.112\ R) \times 10^{-3}\ \text{a.u.}, \tag{14}$$

for $T = 300$ K, and

$$M_{\mathrm{eff}}(R) = (2.104 - 1.087\ R) \times 10^{-3}\ \text{a.u.}, \tag{15}$$

for $T = 5 - 10\ K$, where R is in Å. Our room-temperature transition moment, shown in Fig. 5 (solid line), is seen to pass through the error bars of the points determined from the discrete spectrum and increases as R decreases, as predicted by the *ab initio* calculations.[49] The rate of increase, however, is significantly greater than that calculated by Klotz and Peyerimhoff[49] and also exceeds that implied from a linear least-squares fit to the discrete points.

2. The $A'\ ^3\Delta_u \leftarrow X\ ^3\Sigma_g^-$ transition

In a general treatment of $^3\Delta \leftarrow {}^3\Sigma$ transitions, Kerr and Watson[31] showed that the rotational line strengths are governed by six independent transition moments: one parallel (Z_1) and two perpendicular (Y_1 and Y_2) moments arising from spin-orbit perturbation, and three further perpendicular moments (M_1, M_2 and M_3) arising from low-order orbit-rotation couplings. In the specific case of the $A'\ ^3\Delta_u \leftarrow X\ ^3\Sigma_g^-$ transition of O_2, it was found necessary to retain all six moments in order to explain satisfactorily the observed rotational line strengths,[67] implying some departure from the first-order relations $Z_1 = 0$, $Y_1 = Y_2 = Y$, $M_1 = M_2 = M_3 = M$. Thus, the intensity-borrowing mechanism for the $A' \leftarrow X$ transition may involve perturbations by electronic states of many different symmetries and multiplicities. First-order transition moments for the $A' \leftarrow X$ system arise through interactions involving only $^3\Pi$ intermediaries and, in this approximation, values for Y have been calculated *ab initio* by Klotz and Peyerimhoff.[49]

It follows from the sum rule for the $A' \leftarrow X$ rotational line strengths[31] that the square of the effective electronic transition moment is given by

$$M_{\mathrm{eff}}^2 \propto Z_1^2 + Y_1^2 + Y_2^2 + 2J(J+1)[M_1^2 + M_2^2] + 2(J-1)(J+2)M_3^2. \tag{16}$$

Relative values for the individual transition moments deduced from limited experimental measurements on the (4,0), (7,0) and (9,0) $A' \leftarrow X$ bands[31,35] imply that the first term in Eq. (16) is negligible and that the $A' \leftarrow X$ transition is ~99% perpendicular. Hereafter, we will ignore the small parallel component of this transition.

We determined effective electronic transition moments for the (9,0) and (11,0) $A' \leftarrow X$ bands, shown in Fig. 5 plotted as a function of R-centroid, using the CRDS oscillator strengths of Huestis *et al.*[35] in Eq. (11), together with appropriate Franck-Condon factors calculated using our A'-state potential-energy curve, and transition energies given by Coquart and Ramsay.[30] Neither the precision nor the quantity of experimental data enables any conclusion to be made regarding the R-dependence of the transition moment. Therefore, we assume the relative slope implied by the *ab initio* calculations of Klotz and Peyerimhoff[49] and adopt a linear representation of the $A' \leftarrow X$ effective electronic transition moment, appropriate for room-temperature calculations,

$$M_{\mathrm{eff}}(R) = (3.461 - 1.285\ R) \times 10^{-4}\ \text{a.u.}, \tag{17}$$

shown in Fig. 5. Our adopted moment for low-temperature calculations was obtained by using the individual (7,0)-band transition moments determined by Kerr and Watson[31] in Eq. (16), in order to obtain the ratio between effective moments for $J = 0$ and $J = 11$, and then applying that ratio to the room-temperature moment of Eq. (17). Our adopted effective electronic transition moment for $T = 5 - 10$ K is given by

$$M_{\mathrm{eff}}(R) = (2.793 - 1.037\ R) \times 10^{-4}\ \text{a.u.} \tag{18}$$

3. The $c\ ^1\Sigma_u^- \leftarrow X\ ^3\Sigma_g^-$ transition

Watson[68] has given general treatments of $^1\Sigma^{\pm} \leftarrow {}^3\Sigma^{\pm}$ and $^1\Sigma^{\pm} \leftarrow {}^3\Sigma^{\mp}$ transitions, showing that only a single perpendicular transition moment is necessary for a description of rotational line strengths in $^1\Sigma^- \leftarrow {}^3\Sigma^-$ transitions. Thus, the Herzberg II system, $c\ ^1\Sigma_u^- \leftarrow X\ ^3\Sigma_g^-$, is free of the complexities involved in the triplet-triplet Herzberg I and III systems. To the first order, only spin-orbit interactions contribute to the $c \leftarrow X$ transition moment which is derived from mechanisms of the type:[49]

$$X\ ^3\Sigma_{g,\pm 1}^- \overset{\perp}{\rightarrow} {}^3\Pi_{u,0^-} \overset{\mathrm{SO}}{\leftrightarrow} c\ ^1\Sigma_{u,0^-}^-, \tag{19}$$

and

$$X\ ^3\Sigma_{g,\pm 1}^- \overset{\mathrm{SO}}{\leftrightarrow} {}^1\Pi_{g,\pm 1} \overset{\perp}{\rightarrow} c\ ^1\Sigma_{u,0^-}^-. \tag{20}$$

We have determined effective electronic transition moments for the (13,0), (14,0) and (16,0) $c \leftarrow X$ bands, shown in Fig. 5 plotted as a function of R-centroid, using the CRDS oscillator strengths of Huestis *et al.*[35] in Eq. (11), together with appropriate Franck-Condon factors calculated using our c-state potential-energy curve, and transition energies given by Ramsay.[29] Our adopted effective electronic transition moment for the $c \leftarrow X$ system, shown in Fig. 5, is consistent with these discrete points, but has a relative slope defined by the *ab initio* calculations of Klotz and Peyerimhoff:[49]

$$M_{\mathrm{eff}}(R) = (2.958 - 1.620\ R) \times 10^{-4}\ \text{a.u.} \tag{21}$$

Under the approximation whereby any second-order contributions arising from J-dependent orbit-rotation interactions have been neglected, Eq. (21) is assumed to apply at any temperature.

D. Cross sections

The cross section for photoabsorption from an initial discrete state into a continuum state is given by

$$\sigma(\nu, J) = 1.225 \times 10^{-23} \nu |\langle \chi'_{\nu J}(R) | M_{\mathrm{eff}}(R) | \chi''_{vJ}(R) \rangle|^2\ \mathrm{cm}^2, \tag{22}$$

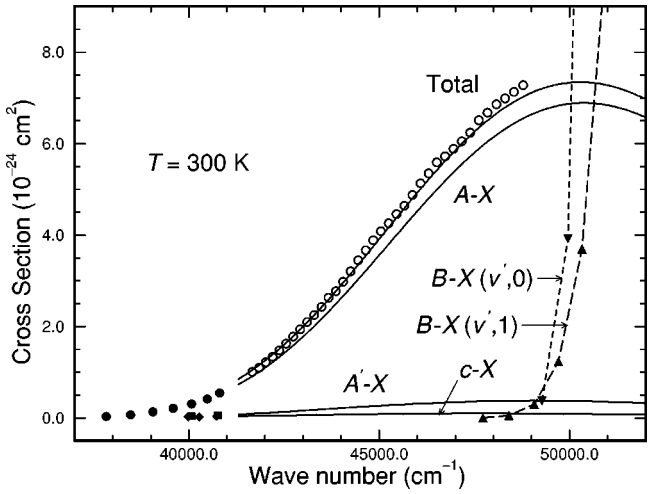

FIG. 6. Room-temperature photoabsorption cross sections in the Herzberg-continuum region. Solid lines: calculated cross sections for the Herzberg I, II, III and total Herzberg continua. Open circles: recommended experimental Herzberg continuum cross section (Ref. 44). Closed symbols: effective cross sections determined for discrete spectra from experimental oscillator-strength densities; $A \leftarrow X$ (4,0)–(10,0) (circles), oscillator strengths from Ref. 50; $A' \leftarrow X$ (9,0), (11,0) (squares) and $c \leftarrow X$ (13,0), (14,0) and (16,0) (diamonds), oscillator strengths from Ref. 35; $B \leftarrow X$ $(v',0)$ (inverted triangles, dashed line) and $(v',1)$ (triangles, long-dashed line), oscillator strengths from Refs. 73 and 74.

where ν is the transition energy in cm^{-1}, $\chi''_{vJ}(R)$ is the normalized discrete radial wavefunction of the initial state, $\chi'_{\nu J}(R)$ is the energy-normalized radial wavefunction of the final continuum state, and $M_{\mathrm{eff}}(R)$ is the effective electronic transition moment, with the transition matrix element evaluated in a.u. Temperature-dependent cross sections may be constructed by calculating cross sections for absorption from all relevant vibrational and rotational levels of the initial state using Eq. (22), weighting with appropriate normalized Boltzmann factors, and adding. Since it is not possible to resolve the structure of the final continuum state, it is unnecessary to consider the true branch structure of the transition and the single Q-branch model implied by Eq. (22) provides an accurate description of the cross section.

Room-temperature photoabsorption cross sections for the Herzberg I, II, III and total continua calculated using this method are shown in Fig. 6 (solid lines). The wavefunctions $\chi''_{vJ}(R)$ were determined by numerical integration of the radial Schrödinger equation for an RKR X-state potential, while the A-, A' and c-state potentials described in Sec. IV B were employed to determine the upper-state wave functions $\chi'_{\nu J}(R)$. As has been described in Sec. IV C, where necessary, effective electronic transition moments $M_{\mathrm{eff}}(R)$ evaluated for $J=11$ were used in calculations of the room-temperature cross sections.

The calculated Herzberg I $(A \leftarrow X)$ cross section reaches a maximum of 6.89×10^{-24} cm^2 at 50 380 cm^{-1} (198 nm), while the Herzberg III $(A' \leftarrow X)$ cross section reaches 0.38×10^{-24} cm^2 at 49 080 cm^{-1} (204 nm) and the Herzberg II $(c \leftarrow X)$ cross section 0.10×10^{-24} cm^2 at 47 680 cm^{-1} (210 nm). The calculated total Herzberg continuum cross section reaches a maximum of 7.35×10^{-24} cm^2 at 50 280 cm^{-1} (199 nm) and is in good agreement with the recommended room-temperature Herzberg continuum cross section of Yoshino *et al.*[44] (open circles), reflecting our chosen method of optimizing the $A \leftarrow X$ transition-moment slope. The calculated total Herzberg continuum cross section is dominated by the Herzberg I contribution which rises from 86% at 41 300 cm^{-1} (242 nm) to 94% at the cross-section maximum. These Herzberg I cross-section branching ratios exceed those implied by the calculations of Saxon and Slanger,[51] which were based principally on the *ab initio* transition moments of Klotz and Peyerimhoff,[49] but, of course, are consistent with the discrete-spectrum branching ratio measured by Huestis *et al.*,[35] on which our adopted transition moments were partially based.

Also shown in Fig. 6 (solid circles, squares and diamonds) are effective cross sections related to the experimental oscillator-strength densities for the discrete Herzberg transitions, determined using the approximate expression

$$\sigma(\nu_{v'0}) = 1.77\times10^{-12} f_{v'0}/(\nu_{v'+1,0} - \nu_{v'-1,0}), \qquad (23)$$

where room-temperature band oscillator strengths $f_{v'0}$ were taken from England *et al.*[50] $(A \leftarrow X)$ and Huestis *et al.*[35] $(A' \leftarrow X$ and $c \leftarrow X)$, and the effective band wavenumbers $\nu_{v'0}$ were taken as the $^QQ_2(11)$ wavenumbers of Yoshino *et al.*[32] $(A \leftarrow X)$, the $^QQ_2(11)$ wavenumbers of Coquart and Ramsay[30] $(A' \leftarrow X)$, and the average of the $R(11)$ and $P(11)$ wavenumbers of Ramsay[29] $(c \leftarrow X)$. The calculated individual Herzberg continuum cross sections are seen to be consistent with the corresponding discrete oscillator-strength densities, reflecting our choice of effective transition moments in Sec. IV C, and as required by the principle of continuity of oscillator-strength density across a dissociation limit.[69] It is worth noting that the experimental (total) Herzberg continuum cross section of Yoshino *et al.*[44] in the dissociation-limit region exceeds a rough extrapolation of the Herzberg I $\sigma(\nu_{v'0})$, within experimental uncertainty, by an amount consistent with the measured Herzberg I cross-section branching ratio of 86%, demonstrating the the mutual compatibility of our chosen experimental data sets for the discrete and continuous spectra. On the other hand, the Herzberg-continuum cross section measured recently by Amoruso *et al.*[46] is $\sim$13% *lower* than the extrapolated Herzberg I $\sigma(\nu_{v'0})$, demonstrating the incompatibility between these data[46] and the best available measurements of the discrete spectrum.[36] This incompatibility has also been commented upon by Yoshino *et al.*[70]

Because of the relatively small contributions of the Herzberg II and III transitions to the total Herzberg continuum, it is the R-dependence of the effective Herzberg I transition moment that has the most important influence on the intensity and shape of the continuum. If, for example, the effective $A \leftarrow X$ transition moment is chosen to have a slope smaller than that of our adopted moment, consistent with a linear least-squares fit to the discrete points in Fig. 5, then the calculated Herzberg I cross section is found to have a maximum of only 5.69×10^{-24} cm^2, some 17% smaller than our calculated maximum $A \leftarrow X$ cross section, at 50 000 cm^{-1} (200 nm), some 2 nm longward of our calculated peak. This difference in cross section is larger than the experimental uncertainty in the Herzberg-continuum cross

section. Therefore, we have determined the final model $A \leftarrow X$ transition-moment slope by requiring that the calculated cross section reproduce approximately the measured cross section in Fig. 6, as foreshadowed in Sec. IV C. Small remaining differences in shape between the calculated and measured Herzberg cross sections suggest that the true $A \leftarrow X$ transition moment may be increasing as R decreases *faster* than linearly. The relative slope of our adopted $A \leftarrow X$ transition moment exceeds that calculated *ab initio* by Klotz and Peyerimhoff[49] for the principal parallel component by a factor of ~ 3. The explanation for this discrepancy remains unclear.[71]

The room-temperature Herzberg continuum is overlapped by the discrete SR ($B \leftarrow X$) transitions for $\nu > 47\,720$ cm^{-1}, inhibiting direct observation of the maximum in the continuum cross section. Therefore, we have considered only the long-wavelength continuum measurements[44] in constructing our absorption model.[72] Effective cross sections related to the room-temperature oscillator-strength densities due to the $(v',0)$ and $(v',1)$ SR bands, shown in Fig. 6 (solid triangles), emphasize the rapid onset of the stronger SR absorption. These cross sections were determined using Eq. (23) with the measured SR oscillator strengths of Lewis *et al.*[73] and Cheung *et al.*,[74] and the band wavenumbers of Yoshino *et al.*[75] and Cheung *et al.*,[74] with extrapolation where necessary. Coquart *et al.*[76] have measured O_2 photoabsorption cross sections for $T = 219$ K in the range 196.4–205 nm, correcting for the effects of SR-band predissociation line wings in obtaining estimates for the Herzberg continuum intensity. Their results imply a cross-section maximum of $8.1-8.2 \times 10^{-24}$ cm^2 in the range 198–199 nm. While this cross section is significantly larger than our calculated value, the position of the maximum is in good agreement. Other Herzberg photoabsorption models[44,76,77] predict cross-section maxima to occur in the range 196–205 nm.

E. Transition character

Having constructed a Herzberg photoabsorption model consistent with the best available experimental information, we are now in a position to consider the predictions of that model regarding the nature of the Herzberg continuum. As we have shown in Sec. IV C, the only significant source of parallel character is the Herzberg I transition. Under this circumstance, the relative perpendicular character of the total Herzberg photoabsorption is given by

$$r_{\mathrm{tot}}^{\perp} = r_{AX}^{\perp} r_{AX} + (1 - r_{AX}), \tag{24}$$

where $r_{AX}^{\perp} = M_{\perp}^2/(M_{\perp}^2 + M_{\parallel}^2)$ is the perpendicular branching ratio of the Herzberg I transition and $r_{AX} = \sigma_{AX}/\sigma_{\mathrm{tot}}$ is the Herzberg I cross-section branching ratio.

In Fig. 7, we show, plotted as a function of the $A \leftarrow X$ R-centroid, values of $r_{AX}^{\perp}$ (open circles) obtained using Eq. (9) with $J = 0$ and the $A \leftarrow X$ transition moments of England *et al.*,[50] obtained from the (4,0)–(10,0) band oscillator-strength measurements of Yoshino *et al.*[36] It can be seen in Fig. 7 that there is a tendency for $r_{AX}^{\perp}$ to increase as R decreases. Our adopted value for this branching ratio in the continuum has been obtained by extrapolation towards shorter R. A weighted least-squares fit to the discrete points yields the result:

$$r_{AX}^{\perp}(R) = 1.159 - 0.593\ R, \tag{25}$$

shown as a solid line in Fig. 7.

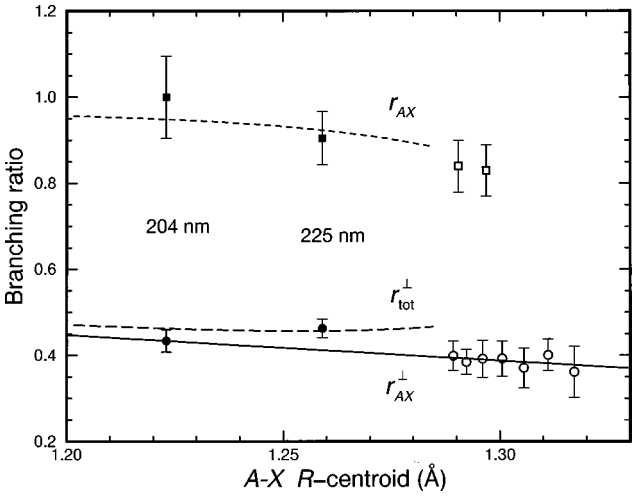

FIG. 7. Low-temperature branching ratios for the Herzberg systems. Open circles: discrete perpendicular branching ratios $r_{AX}^{\perp}$ for the $A \leftarrow X$ (4,0)–(10,0) bands, determined from the transition moments of Ref. 50. Solid line: adopted perpendicular branching ratio for the $A \leftarrow X$ system. Open squares: discrete $A \leftarrow X$ cross-section branching ratios r_{AX} determined from experimental (room-temperature) Herzberg I, II and III oscillator strengths (Refs. 35 and 50). Dashed line: calculated $A \leftarrow X$ cross-section branching ratio for the continuum. Long-dashed line: calculated perpendicular branching ratios $r_{\mathrm{tot}}^{\perp}$ for the total Herzberg continuum. Solid circles: experimental perpendicular branching ratios for the total Herzberg continuum, determined from the current photodissociation angular-distribution measurements. Solid squares: $A \leftarrow X$ cross-section branching ratios for the continuum, inferred from the current experimental perpendicular branching ratios and our adopted perpendicular branching ratio for the $A \leftarrow X$ system.

Also shown in Fig. 7 are values of the Herzberg I cross-section branching ratio r_{AX}, plotted as a function of the $A \leftarrow X$ R-centroid. The discrete points (open squares) were determined using the experimental oscillator-strength densities, described in Sec. IV D, for two regions where there were near coincidences of Herzberg I, II and III transitions. The results, 0.84 ± 0.06 near $40\,740$ cm^{-1}, and 0.83 ± 0.06 near $40\,070$ cm^{-1}, are consistent with the estimate due to Huestis *et al.*[35] of 0.86. Our model value for the Herzberg I cross-section branching ratio (dashed line) was determined following calculation of the Herzberg I, II and III continuum cross sections, using Eq. (22) with $J = 0$ and rotationless forms of the effective transition moments described in Sec. IV C. The model r_{AX}, as required, is consistent with values in the discrete spectrum[78] and rises slowly as R decreases. Finally, values of $r_{\mathrm{tot}}^{\perp}$ for the Herzberg continuum have been determined using our adopted values of $r_{AX}^{\perp}$ and r_{AX} in Eq. (24), and are shown as a long-dashed line in Fig. 7.

V. ANGULAR DISTRIBUTIONS

A. Fine-structure-averaged angular distributions

The photofragment angular distributions measured in this work at $T = 5-10$ K enable the mixture of perpendicular

and parallel character of the total Herzberg continuum to be established independently. It is, therefore, of great interest to compare values of $r_{\mathrm{tot}}^{\perp}$ obtained from these angular distributions with the low-temperature model predictions.

Using the fine-structure-specific angular-distribution parameters measured at 226 nm (Table I), and weighting according to the corresponding dissociation branching ratios, a fine-structure-averaged $\beta=0.612\pm0.065$ is obtained, implying that the dissociation has 54% parallel character ($\beta=2$) and 46% perpendicular character ($\beta=-1$), i.e. $r_{\mathrm{tot}}^{\perp}=0.463\pm0.022$. The corresponding model value is 0.457, in excellent agreement. Since we were unable to determine the dissociation branching ratios at 204 nm, we have estimated the fine-structure-averaged β at this wavelength by assuming that the fine-structure branching is statistical, justifying this assumption by noting that the recoil kinetic energy is $34\times$ the spin-orbit splitting. This is not necessarily a good criterion for the suddenness of the dissociation. Huang *et al.*[11] mention a case where the recoil energy is 28 times the spin-orbit splitting, while the dissociation takes place nearly fully adiabatically. What matters is the characteristic recoil time, which must be short compared with the electronic precession time. In general, this is the case when the recoil energy is large compared with the spin-orbit splitting. From the estimated fine-structure-averaged $\beta=0.699\pm0.077$, it follows that $r_{\mathrm{tot}}^{\perp}=0.434\pm0.026$ at 204 nm, in reasonable agreement with our model value of 0.463. At 236 nm, we were only able to measure the $O(^3P_1)$ angular distribution, from which no conclusion can be drawn. Our experimental $r_{\mathrm{tot}}^{\perp}$ (solid circles) are shown in Fig. 7, compared with the model values, plotted at their respective $A\leftarrow X$ R-centroid values of 1.259 Å (226 nm) and 1.223 Å (204 nm). Tonokura *et al.*[16] have measured the anisotropy parameter for photodissociation of O_2 at 226 nm, together with corresponding fine-structure dissociation branching ratios. Their branching ratios ($^3P_0:{}^3P_1:{}^3P_2=1.0:3.8:9.6$) are in good agreement with ours, but their anisotropy parameter, $\beta=1.6\pm0.4$, differs considerably. Such a high value would imply that the Herzberg continuum has only $\sim13\%$ perpendicular character, well below the known perpendicular branching ratio for the Herzberg I transition alone (Fig. 7). At present, we see no reason to doubt the transition character determined from detailed high-resolution optical rotational line-strength measurements in the discrete $A\leftarrow X$ spectrum. Furthermore, we note that the anisotropy parameter obtained by Tonokura *et al.*[16] was a result of a fitting process to Doppler profiles of photofragments. However, these profiles did not take into account any two-photon contributions, which should yield a broadband background. Our measurements clearly show this strong contribution, and for a reliable determination of the anisotropy parameter this contribution should not be neglected.

It is clear from Fig. 7 that the experimental $r_{\mathrm{tot}}^{\perp}$ are in reasonable agreement with our adopted $r_{AX}^{\perp}$, implying that the Herzberg continuum is dominated by the Herzberg I transition. Herzberg I cross-section branching ratios r_{AX} of 0.91 ± 0.07 (226 nm) and 1.00 ± 0.10 (204 nm), inferred using Eq. (24) with the experimental $r_{\mathrm{tot}}^{\perp}$ and the model $r_{AX}^{\perp}$, are shown in Fig. 7 (solid squares). Within the estimated uncertainty, which takes into account both the experimental uncertainty and the uncertainty involved in the model $r_{AX}^{\perp}$ extrapolation, the ''experimental'' r_{AX} are seen to be in good agreement with the model predictions.

B. Fine-structure-resolved angular distributions

Thus far, we have looked at fine-structure-averaged β parameters at 226 nm and 204 nm to obtain information on the nature of the optical transition, ignoring the fact that each of the $O(^3P_0, {}^3P_1,$ and $^3P_2)$ photofragments has a different angular distribution, a surprising observation in itself. In this section, we focus on the individual angular distributions of the three fine-structure states. It is difficult to perform accurate calculations on these fine-structure-specific angular distributions without an intimate knowledge of the angular-momentum couplings of the electronic states participating in the transition, and the small- and large-R interactions with other states. Therefore, we restrict our considerations to the approximate cases defined by a case (a) description of the molecular states and adiabatic and sudden-recoil limits for the molecular dissociation dynamics. The approximations used make us very cautious in the drawing of conclusions. However, some qualitative features, such as the fine-structure dependence of the β-parameter in the case of a statistical dissociation, are of interest.

1. Adiabatic limit

From the adiabatic correlation diagram for $O(^3P)+O(^3P)$,[11] it can be seen that all three Herzberg states correlate with $O(^3P_2)+O(^3P_2)$. However, in our experiment we observe the formation of $^3P_1$ and $^3P_0$ fragments at 226 and 204 nm, and $^3P_1$ fragments at 236 nm. The presence of these fragments is inconsistent with adiabatic dissociation behavior.

It is easy to predict the angular distribution of the $^3P_2$ fragments measured at 226 and 204 nm in the case of adiabatic dissociation. Because only one type of fragment is formed in the adiabatic limit, the angular distribution reflects directly the mixed parallel-perpendicular character of the total Herzberg photoabsorption. Using the model of Sec. IV E to describe the relative perpendicular character of the Herzberg system, we find for the adiabatic anisotropy parameter:

$$\beta_{j=2}=r_{\mathrm{tot}}^{\perp}\beta^{\perp}+(1-r_{\mathrm{tot}}^{\perp})\beta^{\parallel}=2-3r_{\mathrm{tot}}^{\perp}, \tag{26}$$

where $\beta^{\perp}=-1$ and $\beta^{\parallel}=2$. From Sec. V A, the model $r_{\mathrm{tot}}^{\perp}=0.457$ at 226 nm and 0.463 at 204 nm. Thus, Eq. (26) gives $\beta_{j=2}=0.629$ and 0.611, respectively, at these two wavelengths. From Table I, the measured $\beta_{j=2}$ at 226 nm is 0.64 ± 0.08, in good agreement with the calculated adiabatic value. This agreement for $O(^3P_2)$ reflects the fact that this is the dominant fragmentation product, which contains the average information on the character of the dissociation. In this sense, the β-parameter for a dominant dissociation product provides a less sensitive indicator of the dissociation adiabaticity than do the dissociation branching ratios. Our experimental results show that the minority channels may have

TABLE II. Fine-structure branching ratios of $O(^3P_j)$, $j=0,1,2$, calculated in the sudden-recoil approximation, following excitation of O_2 into the $A\ ^3\Sigma_{u,\Omega}(\Omega=0^-,\Omega=\pm1)$ sub-states. The parameters p and q are clarified in the text.

	$j=0$	$j=1$	$j=2$
$\Omega=0^-$	$4q$	$6p+6q$	$6p+14q$
$\Omega=\pm1$	$2p+2q$	$3p+9q$	$7p+13q$

very different anisotropy parameters. The fact that the measured β-parameter for $O(^3P_2)$ at 204 nm (0.87 ± 0.10) differs significantly from the adiabatic value suggests that the distribution over the fine-structure levels at this wavelength may not be as dominated by the $j=2$ fragments.

2. Sudden-recoil limit

The other extreme is the prompt dissociation process, described in the sudden-recoil limit. It is commonplace for a prompt dissociation to result in a statistical, or nearly statistical distribution over fine-structure states. The distribution can deviate from statistical when the optical excitations to the different molecular fine-structure states are of different strengths. Another exception occurs when it is not possible to conserve Ω in the dissociation process.[8] This is, for example, the case for the $A'\ ^3\Delta_u(\Omega=3)$ state that cannot connect to $^3P_0$ in any combination of $O(^3P_0)+O(^3P_j)$. As has been shown by Singer *et al.*,[8] the sudden-recoil case can be treated by writing the molecular wave function as a linear combination of atomic eigenstates, the suddenness of the dissociation ''freezing'' the angular part of the wavefunction. The squared coefficients in this expansion determine the branching over the different atomic fine-structure states. In Table II, derived from Table IV of Ref. 12, we collect these branching ratios for the A state. The coefficients p and q in Table II refer to so-called eigenvector coefficients $\langle\lambda_a\lambda_b|\Lambda\rangle$, factors that are used in the expansion of the orbital part of the molecular eigenstate $|\Lambda\rangle=|0\rangle$ into the orbital part of the atomic eigenstates $|l_a=1,\lambda_a\rangle$ and $|l_b=1,\lambda_b\rangle$: $p=\langle00|0\rangle$ and $q=\langle\pm1\mp1|0\rangle$. Calculation of these factors is not a straightforward process and we will use them as adjustable parameters, under the one restriction that the sum of each row in Table II is unity. This reflects that for $\Omega=0$, 1, and -1, the dissociation probability is unity $(12p+24q\equiv1)$.

From an orientational point of view, two classes of molecules are formed following excitation of O_2 in the Herzberg continuum. On the one hand, molecules excited by perpendicular transitions into the electronic states $c\ ^1\Sigma_u^-$, $A'\ ^3\Delta_u$, and $A\ ^3\Sigma^+_{u,0^-}$ dissociate with an anisotropy parameter $\beta=\beta^\perp$. On the other hand, molecules are excited into the $A\ ^3\Sigma^+_{u,\pm1}$ states through transitions of mixed parallel and perpendicular character: we will label the corresponding anisotropy parameter $\beta^{\pm1}_{AX}$. The dissociation process influences the relative contributions of these two classes of molecules to specific atomic fine-structure states. Thus, in general, the $O(^3P_0,\ ^3P_1,$ and $^3P_2)$ photofragments may have different angular distributions. These fine-structure-specific angular distributions, as well as the fine-structure dissociation branching ratios, can be used, in principle, to obtain information on the correlation between molecular and atomic fine-structure levels, helping to elucidate the (a)diabaticity of the dissociation process.

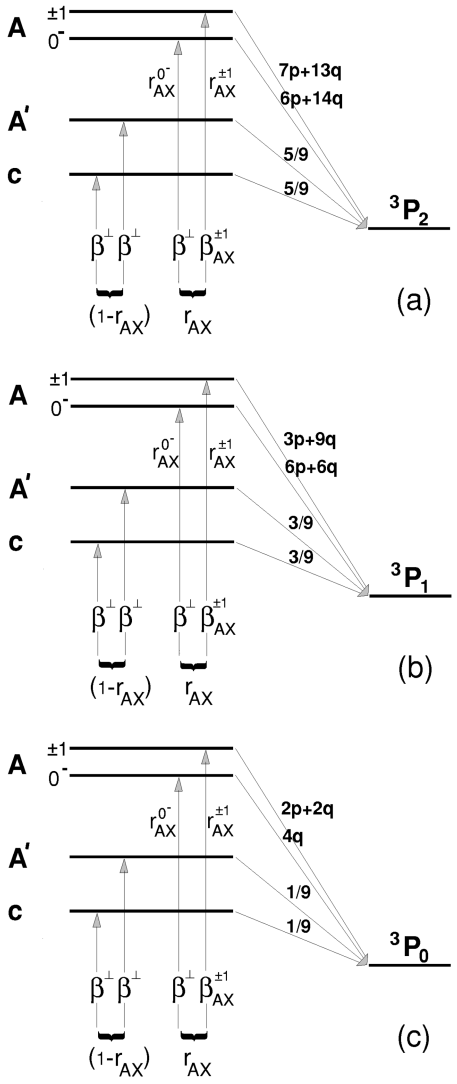

FIG. 8. Schematic diagrams used for the calculation of fine-structure-resolved angular distributions of $O(^3P_j)$ atoms resulting from photodissociation of O_2 in the Herzberg continuum. Indicated are the three Herzberg states A, A', and c. Transitions from the O_2 ground state to the $A(\Omega=0^-)$, A', and c states are perpendicular $(\beta=-1)$, while the transition to the $A(\Omega=\pm1)$ state is of mixed parallel-perpendicular character. In panels (a), (b), and (c), the sudden-recoil limit is depicted where $^3P_2$ [panel (a)], $^3P_1$ [panel (b)], and $^3P_0$ [panel (c)] atoms are formed. For clarity, (a), (b), and (c) have not been incorporated into one scheme. The symbols are clarified in the text.

In Figs. 8(a)–8(c), we depict schematically the branching for the sudden-recoil dissociation forming $^3P_2$, $^3P_1$, and $^3P_0$ atomic fragments. The Ω-states of the molecule are shown only for the A state, because for this state different Ω-states are associated with different β parameters. The cross-section branching ratios for the $A(\Omega=0^-)$ and $A(\Omega=\pm1)$ states have been labelled $r^{0^-}_{AX}$ and $r^{\pm1}_{AX}$, respectively. Furthermore, we make the approximation that the A'-

and c-state dissociations result in a statistical fine-structure distribution. Using the notation adopted in Figs. 8(a)–8(c), we find:

$$\beta_{j=0}=\frac{r_{AX}r_{AX}^{0^-}(4q)\beta^{\perp}+r_{AX}r_{AX}^{\pm 1}(2p+2q)\beta_{AX}^{\pm 1}+\frac{1}{9}(1-r_{AX})\beta^{\perp}}{r_{AX}r_{AX}^{0^-}(4q)+r_{AX}r_{AX}^{\pm 1}(2p+2q)+\frac{1}{9}(1-r_{AX})}, \tag{27}$$

$$\beta_{j=1}=\frac{r_{AX}r_{AX}^{0^-}(6p+6q)\beta^{\perp}+r_{AX}r_{AX}^{\pm 1}(3p+9q)\beta_{AX}^{\pm 1}+\frac{3}{9}(1-r_{AX})\beta^{\perp}}{r_{AX}r_{AX}^{0^-}(6p+6q)+r_{AX}r_{AX}^{\pm 1}(3p+9q)+\frac{3}{9}(1-r_{AX})}, \tag{28}$$

and

$$\beta_{j=2}=\frac{r_{AX}r_{AX}^{0^-}(6p+14q)\beta^{\perp}+r_{AX}r_{AX}^{\pm 1}(7p+13q)\beta_{AX}^{\pm 1}+\frac{5}{9}(1-r_{AX})\beta^{\perp}}{r_{AX}r_{AX}^{0^-}(6p+14q)+r_{AX}r_{AX}^{\pm 1}(7p+13q)+\frac{5}{9}(1-r_{AX})}. \tag{29}$$

In order to calculate these sudden-recoil anisotropy parameters, it is convenient to express $r_{AX}^{0^-}$ and $r_{AX}^{\pm 1}\beta_{AX}^{\pm 1}$ in terms of $r_{AX}^{\perp}$, for which a model has been constructed in Sec. IV E. Using Table I of Ref. 61, it is possible to deduce sum rules for transitions into the $A(\Omega=0^-)$ and $A(\Omega=\pm 1)$ states. Under the approximation that rotational terms contributing to the transition moment may be neglected at the low beam temperature appropriate to this work, and neglecting M compared with Z and Y, it follows that $r_{AX}^{0^-}=2Y^2/(Z^2+4Y^2)=1-r_{AX}^{\pm 1}$. From this relation, Eq. (9) and the definition of $r_{AX}^{\perp}$ in Sec. IV E, it follows that $r_{AX}^{0^-}=\frac{1}{2}r_{AX}^{\perp}=1-r_{AX}^{\pm 1}$. Using alternative expressions for the average β parameter for the $A\leftarrow X$ transition, we can write $r_{AX}^{0^-}\beta^{\perp}+r_{AX}^{\pm 1}\beta_{AX}^{\pm 1}=r_{AX}^{\perp}\beta^{\perp}+(1-r_{AX}^{\perp})\beta^{\parallel}=2-3r_{AX}^{\perp}$. Thus, $r_{AX}^{\pm 1}\beta_{AX}^{\pm 1}=(2-\frac{5}{2}r_{AX}^{\perp})$. Accordingly, Eqs. (27)–(29) become:

$$\beta_{j=0}=\frac{-\frac{1}{2}r_{AX}r_{AX}^{\perp}(4q)+r_{AX}(2-\frac{5}{2}r_{AX}^{\perp})(2p+2q)-\frac{1}{9}(1-r_{AX})}{\frac{1}{2}r_{AX}r_{AX}^{\perp}(4q)+r_{AX}(1-\frac{1}{2}r_{AX}^{\perp})(2p+2q)+\frac{1}{9}(1-r_{AX})}, \tag{30}$$

$$\beta_{j=1}=\frac{-\frac{1}{2}r_{AX}r_{AX}^{\perp}(6p+6q)+r_{AX}(2-\frac{5}{2}r_{AX}^{\perp})(3p+9q)-\frac{3}{9}(1-r_{AX})}{\frac{1}{2}r_{AX}r_{AX}^{\perp}(6p+6q)+r_{AX}(1-\frac{1}{2}r_{AX}^{\perp})(3p+9q)+\frac{3}{9}(1-r_{AX})}, \tag{31}$$

and

$$\beta_{j=2}=\frac{-\frac{1}{2}r_{AX}r_{AX}^{\perp}(6p+14q)+r_{AX}(2-\frac{5}{2}r_{AX}^{\perp})(7p+13q)-\frac{5}{9}(1-r_{AX})}{\frac{1}{2}r_{AX}r_{AX}^{\perp}(6p+14q)+r_{AX}(1-\frac{1}{2}r_{AX}^{\perp})(7p+13q)+\frac{5}{9}(1-r_{AX})}. \tag{32}$$

Model values for both r_{AX} and $r_{AX}^{\perp}$ can be obtained from Fig. 7 for the different wavelengths of interest. We have used a least-squares procedure, varying the parameters p and q, to optimize our calculated β-parameters with respect to the measured values. Best agreement was obtained with $p=0.009$ and $q=0.037$. We have listed the calculated β-parameters in Table III. Comparing these values with the measured values in Table I, we can draw the following conclusions. At 236 nm, the dissociation is not of the sudden-recoil type, since the calculated $\beta_{j=1}=0.70$ is well outside the error bar of the measured value of 0.31 ± 0.15. In addition, at 204 nm the dissociation is still not sudden: although the calculated $\beta_{j=0}$ value falls within the error bar of the measured value, the measured and calculated $\beta_{j=1}$ and $\beta_{j=2}$ values are in disagreement. One would expect more parallel character in the observed $^3P_1$ angular distribution and more perpendicular character for $^3P_2$, in the case of a sudden-recoil dissociation. Hence it is likely that, also in the intermediate regime at 226 nm, the dissociation will not be in the sudden-recoil limit. Therefore, the relatively good agreement between the calculated and measured anisotropy parameters at this wavelength must be considered as fortuitous. This conclusion also follows, of course, from the nonstatistical fine-structure distribution observed at this wavelength.

We have also calculated the dissociation branching ratios over the fine-structure states, using the denominators of Eqs. (30)–(32). Normalizing the distribution on the $j=0$ intensity, we find the values collected in Table IV, which are not completely statistical. As remarked previously, sudden-recoil distributions can deviate from a perfect statistical distribution. However, these small calculated deviations cannot

TABLE III. Anisotropy parameters, calculated in the sudden-recoil approximation, characterizing the angular distribution of $O(^3P_j)$, $j=0,1,2$, photofragments formed in the excitation of the O_2 Herzberg continuum.

λ nm	β $j=0$	$j=1$	$j=2$
204	0.42	0.70	0.58
226	0.43	0.71	0.61
236	0.43	0.70	0.60

TABLE IV. Branching ratios, calculated in the sudden-recoil approximation, for $O(^3P_j)$, $j=0,1,2$, formation, following excitation of O_2 in the Herzberg continuum.

λ	Branching ratio		
nm	$j=0$	$j=1$	$j=2$
204	1.0	3.3	5.3
226	1.0	3.3	5.3
236	1.0	3.3	5.3

explain the large deviation from a statistical distribution measured at 226 nm.

The approximate limiting calculations performed above suggest that the dissociation process is neither sudden nor fully adiabatic at the three wavelengths under consideration. Not being in one of the limiting cases, we need accurate knowledge of the couplings between different electronic states at short and large internuclear separation for the calculation of the β-parameters. From an adiabatic correlation diagram,[11] it can be seen which electronic states may be involved in the formation of $j<2$ atoms. The *ungerade* electronic states producing $O(^3P_0)$ are the $^5\Pi_u$ and 2 $^3\Sigma_u^+$ states, while $O(^3P_1)$ can be formed by interaction with $^{1,3,5}\Pi_u$, $^5\Sigma_u^-$, and 2 $^3\Sigma_u^+$ states. Theoretical calculations of the coupling strengths between the Herzberg states and these states are outside the scope of this paper.

VI. CONCLUSIONS

Velocity-map imaging has been used to measure $O(^3P_j)$, $j=0$, 1, and 2 atom angular distributions arising from the photodissociation of molecular oxygen at several wavelengths across the Herzberg continuum. The high image quality afforded by the method has allowed the determination of anisotropy parameters, even for such extremely weak transitions as those involved in the Herzberg systems. Previous attempts to obtain this information using Doppler-profile measurements[16] were possibly obstructed by strong signals arising from two-photon absorption, which have been observed clearly in this study.

We have described how photofragment angular distributions are related to the composition of the electronic transition moment between the ground state and the Herzberg continuum of molecular oxygen. The different components contributing to the oscillator strength of the Herzberg continuum can be established by extrapolation of parameters measured for the three Herzberg band systems. To this aim, a review of the current state of knowledge of these transitions has been given. This procedure has allowed for an independent determination of the relative Herzberg I cross section contribution (r_{AX}) to the total Herzberg continuum. The Herzberg I contribution is clearly dominant, rising from 86% at 242 nm to 94% at 198 nm. These numbers exceed the values implied by *ab initio* calculations.[49] Using the same parameters as in the cross-section calculations, the mixed parallel-perpendicular nature of the Herzberg I continuum ($r_{AX}^{\perp}$) and the total Herzberg continuum ($r_{\mathrm{tot}}^{\perp}$) have been determined.

The value of $r_{\mathrm{tot}}^{\perp}$ is crucial, because this quantity can be related to our photofragment angular-distribution measurements, providing an independent check on the quality of the Herzberg photoabsorption model. Comparing the model $r_{\mathrm{tot}}^{\perp}$ with two values obtained from our angular-distribution measurements, we found excellent agreement at 226 nm, and reasonable agreement at 204 nm. The slight discrepancy at 204 nm does not bring the photoabsorption model into dispute since we were unable to measure the branching over the fine-structure states of the atomic fragments at that wavelength and assumed the branching to be statistical, to get a better model. Thus, these two measurements add to the credibility of the model developed to explain the oscillator strength of the Herzberg continuum, but it is clear that more accurate angular-distribution measurements would allow the development of a significantly improved model.

Finally, we have attempted to understand the implications of our fine-structure-resolved angular distributions. Using our knowledge of the character the Herzberg transitions, and making various approximations and assumptions on the (a)diabaticity of the dissociation process, we have found that neither a fully adiabatic, nor a sudden-dissociation process could explain our observations at 204 and 226 nm. Apparently, the diabatic couplings at short R and the nonadiabatic coupling between the adiabatic potential-energy curves at large R play essential roles in the dissociation process, inhibiting both fully adiabatic and fully diabatic behavior. The measured anisotropy parameters will serve as a stringent test for any theoretical calculations that might be performed on the O_2 potential-energy curves and couplings in this region.

ACKNOWLEDGMENTS

This work is part of the research program of the ''Stichting voor Fundamenteel Onderzoek der Materie (FOM),'' which is financially supported by the ''Nederlandse Organisatie voor Wetenschappelijk Onderzoek (NWO).'' The authors wish to thank T. G. Slanger and D. L. Huestis for critical comments on the manuscript, and Cor Sikkens and Eugène van Leeuwen for technical support.

[1] G. Herzberg, Naturwissenschaften **20**, 577 (1932).
[2] G. Herzberg, Can. J. Phys. **30**, 185 (1952).
[3] G. Herzberg, Can. J. Phys. **31**, 657 (1953).
[4] R. R. Meier, Space Sci. Rev. **58**, 1 (1991).
[5] M. Nicolet and R. Kennes, Planet. Space Sci. **34**, 1043 (1986).
[6] A. J. Blake and D. G. McCoy, J. Quant. Spectrosc. Radiat. Transf. **38**, 113 (1987).
[7] G. Ya. Zelikina, V. V. Bertsev, and M. B. Kiseleva, Opt. Spectrosc. **77**, 513 (1994).
[8] S. J. Singer, K. F. Freed, and Y. B. Band, J. Chem. Phys. **79**, 6060 (1983).
[9] S. J. Singer, K. F. Freed, and Y. B. Band, J. Chem. Phys. **81**, 3091 (1984).
[10] L. L. Vahala, P. S. Julienne, and M. D. Havey, Phys. Rev. A **34**, 1856 (1986).
[11] Y.-L. Huang and R. J. Gordon, J. Chem. Phys. **94**, 2640 (1991).
[12] Y. Matsumi and M. Kawasaki, J. Chem. Phys. **93**, 2481 (1990).
[13] A. T. J. B. Eppink, D. H. Parker, M. H. M. Janssen, B. Buijsse, and W. J. van der Zande, J. Chem. Phys. **108**, 1305 (1998).
[14] D. J. Leahy, D. R. Cyr, D. L. Osborn, and D. M. Neumark, Chem. Phys. Lett. **216**, 503 (1993).
[15] D. J. Leahy, D. L. Osborn, D. R. Cyr, and D. M. Neumark, J. Chem. Phys. **103**, 2495 (1995).
[16] K. Tonokura, N. Shafer, Y. Matsumi, and M. Kawasaki, J. Chem. Phys. **95**, 3394 (1991).

[17] A. J. R. Heck and D. W. Chandler, Annu. Rev. Phys. Chem. **46**, 335 (1995).
[18] A. T. J. B. Eppink and D. H. Parker, Rev. Sci. Instrum. **68**, 3477 (1997).
[19] D. H. Parker and A. T. J. B. Eppink, J. Chem. Phys. **107**, 2357 (1997).
[20] C. J. Dash, Appl. Opt. **31**, 1146 (1992).
[21] W. K. Bischel, B. E. Perry, and D. R. Crosley, Appl. Opt. **21**, 1419 (1982).
[22] J. Bamford, L. E. Jusinski, and W. K. Bischel, Phys. Rev. A **34**, 185 (1986).
[23] R. P. Saxon and J. Eichler, Phys. Rev. A **34**, 199 (1986).
[24] Y.-L. Huang and R. J. Gordon, J. Chem. Phys. **93**, 868 (1990).
[25] R. J. Yokelson, R. J. Lipert, and W. A. Chupka, J. Chem. Phys. **97**, 6153 (1992).
[26] This observation is consistent with the results of van der Zande *et al.* [Chem. Phys. Lett. **140**, 175 (1987)] who found qualitatively similar branching in the predissociation of $O_2(3s\sigma\ ^3\Pi_g)$. It is likely that the lowest two valence states of $^3\Pi_g$ symmetry are responsible for the predissociation of both systems. The weaker predissociation to the lower limit supports diabatic behavior at the avoided crossing between the two valence states.
[27] T. G. Slanger and P. C. Cosby, J. Phys. Chem. **92**, 267 (1988).
[28] P. M. Borrell, P. Borrell, and D. A. Ramsay, Can. J. Phys. **64**, 721 (1986).
[29] D. A. Ramsay, Can. J. Phys. **64**, 717 (1986).
[30] B. Coquart and D. A. Ramsay, Can. J. Phys. **64**, 726 (1986).
[31] C. M. L. Kerr and J. K. G. Watson, Can. J. Phys. **64**, 36 (1986).
[32] K. Yoshino, J. E. Murray, J. R. Esmond, Y. Sun, W. H. Parkinson, A. P. Thorne, R. C. M. Learner, and G. Cox, Can. J. Phys. **72**, 1101 (1994).
[33] T. G. Slanger, D. L. Huestis, P. C. Cosby, H. Naus, and G. Meijer, J. Chem. Phys. **105**, 9393 (1996).
[34] The $\Omega=3$ component of the $A'\ ^3\Delta_u$ state is known, from absorption spectra, only for $v=4-11$.
[35] D. L. Huestis, R. A. Copeland, K. Knutsen, T. G. Slanger, R. T. Jongma, M. G. H. Boogaarts, and G. Meijer, Can. J. Phys. **72**, 1109 (1994).
[36] K. Yoshino, J. R. Esmond, J. E. Murray, W. H. Parkinson, A. P. Thorne, R. C. M. Learner, and G. Cox, J. Chem. Phys. **103**, 1243 (1995).
[37] Although the CRDS oscillator strengths for the $A\leftarrow X$ system are ~40% lower than the UVFTS values, Huestis *et al.* (Ref. 35) use recommended values close to those of Yoshino *et al.* (Ref. 36) in estimating the Herzberg I cross-section branching ratio. CRDS oscillator strengths for the weaker $A'\leftarrow X$ and $c\leftarrow X$ systems are expected to be significantly more accurate than those for the $A\leftarrow X$ system.
[38] J. E. Frederick and J. E. Mentall, Geophys. Res. Lett. **9**, 461 (1982).
[39] J. R. Herman and J. E. Mentall, J. Geophys. Res. **87**, 8967 (1982).
[40] G. P. Anderson and L. A. Hall, J. Geophys. Res. **88**, 6801 (1983).
[41] A. S.-C. Cheung, K. Yoshino, W. H. Parkinson, S. L. Guberman, and D. E. Freeman, Planet. Space Sci. **34**, 1007 (1986).
[42] A. Jenouvrier, B. Coquart, and M. F. Merienne, Planet. Space Sci. **34**, 253 (1986).
[43] A. Jenouvrier, B. Coquart, and M. F. Merienne, J. Quant. Spectrosc. Radiat. Transf. **36**, 349 (1986).
[44] K. Yoshino, A. S.-C. Cheung, J. R. Esmond, W. H. Parkinson, D. E. Freeman, S. L. Guberman, A. Jenouvrier, B. Coquart, and M. F. Merienne, Planet. Space Sci. **36**, 1469 (1988).
[45] K. Yoshino, J. R. Esmond, A. S.-C. Cheung, D. E. Freeman, and W. H. Parkinson, Planet. Space Sci. **40**, 185 (1992).
[46] A. Amoruso, L. Crescentini, M. S. Cola, and G. Fiocco, J. Quant. Spectrosc. Radiat. Transf. **56**, 145 (1996).
[47] H. Partridge, C. W. Bauschlicher, Jr., S. R. Langhoff, and P. R. Taylor, J. Chem. Phys. **95**, 8292 (1991).
[48] R. P. Saxon and B. Liu, J. Chem. Phys. **67**, 5432 (1977).
[49] R. Klotz and S. D. Peyerimhoff, Mol. Phys. **57**, 573 (1986).
[50] J. P. England, B. R. Lewis, and S. T. Gibson, Can. J. Phys. **74**, 185 (1996).
[51] R. P. Saxon and T. G. Slanger, J. Geophys. Res. **91**, 9877 (1986).
[52] D. R. Bates, Planet. Space Sci. **36**, 869 (1988).
[53] In this paper, potential energy, in eV, is referred to the minimum in the ground-state $X\ ^3\Sigma_g^-$ potential-energy curve.
[54] Except for the highest vibrational levels of the A state, which are perturbed significantly, our RKR procedure reproduces the experimental G_v and B_v values to within $0.7\ \mathrm{cm}^{-1}$ and $5\times10^{-4}\ \mathrm{cm}^{-1}$, respectively, for each of the A, A', and c states.
[55] Extrapolation to $v=-0.5$ was performed by fitting a low-order Dunham polynomial to the lowest four known vibrational levels.
[56] R. J. LeRoy, J. Chem. Phys. **73**, 6003 (1980).
[57] P. C. Cosby and D. L. Huestis, J. Chem. Phys. **97**, 6108 (1992).
[58] S. S. Banerjee, Ph.D. dissertation thesis, The Australian National University, 1997.
[59] B. R. Lewis, S. S. Banerjee, and S. T. Gibson, J. Chem. Phys. **102**, 6631 (1995).
[60] Experimental information on the Rydberg-valence interaction for $^3\Delta_u$ symmetry can be obtained from the measured photoabsorption spectrum of metastable $O_2(a^1\Delta_g)$ (P. C. Hill, Ph.D. dissertation thesis, The Australian National University, 1991), but the predissociation pattern of the $^3\Delta_u$ Rydberg state is not well enough defined to enable an accurate repulsive limb of the $A'\ ^3\Delta_u$ state to be established. As far as can be determined, the A'-state potential-energy curve adopted here is consistent with the observed predissociation of the $^3\Delta_u$ Rydberg state. No experimental information is available on the Rydberg state of $^1\Sigma_u^-$ symmetry.
[61] V. P. Bellary and T. K. Balasubramanian, J. Quant. Spectrosc. Radiat. Transf. **45**, 283 (1991).
[62] Subscripts in the transition-moment notation adopted in this work refer to the value of Ω'. Equalities between the moments arise because of symmetry considerations, leading to the need for only three independent moments in the case of the $A\leftarrow X$ transition.
[63] Expressions given in Ref. 61 have been simplified and corrected to obtain Eqs. (8) and (9).
[64] P. A. Fraser, Can. J. Phys. **32**, 515 (1954).
[65] D. L. Huestis, in *Atomic, Molecular, and Optical Physics Handbook*, edited by G. W. F. Drake (AIP, New York, 1996), p. 403.
[66] $A\leftarrow X$ R-centroids associated with continuum wavelengths in Fig. 5 are determined using Eq. (13) with the radial part of the A-state continuum wavefunction replacing $\chi_{v'}(R)$.
[67] The rotational line strengths employed by Kerr and Watson (Ref. 31) were taken from the photographically recorded spectra of Coquart and Ramsay (Ref. 30).
[68] J. K. G. Watson, Can. J. Phys. **46**, 1637 (1968).
[69] A. C. Allison and A. Dalgarno, J. Chem. Phys. **55**, 4342 (1971).
[70] K. Yoshino, D. L. Huestis, and R. W. Nicholls, J. Quant. Spectrosc. Radiat. Transfer (to be published).
[71] In principle, it is possible to match the experimental cross section by making adjustments to the A-state potential-energy curve while retaining a smaller transition-moment slope. However, potential-energy curves determined in this way either exhibit anomalies in shape or are inconsistent with the known form in the Rydberg-valence region (Sec. IV B).
[72] We have made very minor corrections to the recommended continuum cross sections of Ref. 44 for $\nu>47\ 720\ \mathrm{cm}^{-1}$ to allow for the effects of the lowest $B\leftarrow X$ hot bands.
[73] B. R. Lewis, L. Berzins, and J. H. Carver, J. Quant. Spectrosc. Radiat. Transf. **36**, 209 (1986).
[74] A. S.-C. Cheung, K. Yoshino, W. H. Parkinson, and D. E. Freeman, Can. J. Phys. **62**, 1752 (1984).
[75] K. Yoshino, D. E. Freeman, and W. H. Parkinson, J. Phys. Chem. Ref. Data **13**, 207 (1984).
[76] B. Coquart, M. F. Merienne, and A. Jenouvrier, Planet. Space Sci. **38**, 287 (1990).
[77] M. Nicolet and R. Kennes, Planet. Space Sci. **36**, 1069 (1988), and references therein.
[78] Strictly speaking, since the discrete cross-section branching ratios are derived from room-temperature measurements and the model r_{AX} is calculated for $J=0$, the strong J-dependence of the $A'\leftarrow X$ transition moment leads to a small discrepancy (~2%).